ADVANCED FUNCTIONAL MATERIALS
www.afm-journal.de

Hydrogel Cryo-Microtomy Continuously Making Soft Electronic Devices

Xuemei Fu, Jiaxin Li, Chengqiang Tang, Songlin Xie, Xuemei Sun, Bingjie Wang, and Huisheng Peng**

Standard fabrication of soft electronic devices with both high controllability and yield is highly desirable but remains a challenge due to the modulus mismatch of component materials through a one-step process. Here, by mimicking the freeze-section process of multicomponent biological tissues containing low-modulus muscles and high-modulus bones, for the first time, a hydrogel cryo-microtomy method to continuously making soft electronic devices based on a sol-solid-gel transition mechanism is presented. Polyvinyl alcohol (PVA) electrolyte and aligned nitrogen-doped multi-walled carbon nanotube (N-MWCNT) array electrode are demonstrated as low- and high-modulus components to fabricate soft supercapacitors with high performances. Stable interfaces form between frozen PVA electrolyte and N-MWCNT electrodes with matched moduli at subzero temperature and are well maintained during cryo-microtomy process. The resulting soft supercapacitors realize controllable patterns, tunable thicknesses from 0.5 to 600 µm, high yields such as 20 devices per minute even at lab scale, and high reproducibility with over 75% devices in 15% performance fluctuation. This cryo-microtomy method is further generalized to fabricate other soft devices such as sensors with high sensing properties.

1. Introduction

Soft electronic devices are rising as they can form stable and atraumatic interfaces with soft, wet, and dynamic biological tissues.[1–5] Typically, soft electronic devices rely on the integration of low-modulus components such as polymer elastomer and hydrogel with moduli on the scale from 10^3 to 10^6 Pa, and high-modulus components such as electrodes based on metal, metal oxide, or carbon nanomaterials with moduli above 10^9 Pa. Moreover, soft electronic devices are expected to be thin enough to render the device-tissue interface as seamless as possible to reduce disturbance.[6,7] It is common to deposit high-modulus materials on low-modulus substrate or decorate electronic devices with low-modulus cladding to endow conventional electronic devices with softness.[8–12] However, it is challenging to make soft electronic devices with both high controllability and yield at one step needed for practical applications, because low-modulus components easily deform with varying microstructures during processing although high-modulus components do not, resulting in unstable interfaces between them during fabrication.

In the food industry, biological tissues consisting of low-modulus components (e.g., muscle) and high-modulus components (e.g., bone) often need sectioning into small units before serving. As a matter of experience, these inhomogeneous biological tissues are frozen to harden the low-modulus components at subzero temperatures before fixing and sectioning. In this case, the low-modulus components penetrate into the high-modulus ones so the whole tissues reach a relatively homogeneous high-modulus state after freezing. As a result, they can be sectioned into small units including cubes, bars, and slices with well-maintained interfaces among different components (**Figure 1**a). Such a strategy holds the prospect to inspire the standard fabrication of soft electronic devices but has not been realized yet.

Herein, we put forward a hydrogel cryo-microtomy method to make soft electronic devices with both high controllability and yield, by penetrating high-modulus electrodes with low-modulus electrolyte and then freezing the interpenetrated network for sectioning into soft electronic devices. As a demonstration, aligned N-MWCNT array electrode and polyvinyl alcohol (PVA) electrolyte were selected as high-modulus and low-modulus components, respectively, for the standard fabrication of soft supercapacitors (Figure 1b–d). Stable interfaces formed between frozen PVA electrolyte and N-MWCNT electrodes with matched moduli at subzero temperature and were well maintained during cryo-microtomy process. It contributed to intact supercapacitor slice at the frozen state (Figure 1c) and stable interfaces after thawing at room temperature (Figure 1d and Figure S1, Supporting Information). The specific capacitances of over 75% obtained soft supercapacitors distributed in the range of 15% fluctuation; their thicknesses were tunable from 0.5 to 600 µm and they were able to be continuously produced

---

Dr. X. Fu, J. Li, C. Tang, Dr. S. Xie, Prof. X. Sun, Prof. B. Wang, Prof. H. Peng
State Key Laboratory of Molecular Engineering of Polymers
Department of Macromolecular Science
and Laboratory of Advanced Materials
Fudan University
Shanghai 200438, China
E-mail: wangbingjie@fudan.edu.cn; penghs@fudan.edu.cn

The ORCID identification number(s) for the author(s) of this article can be found under https://doi.org/10.1002/adfm.202008355.

DOI: 10.1002/adfm.202008355

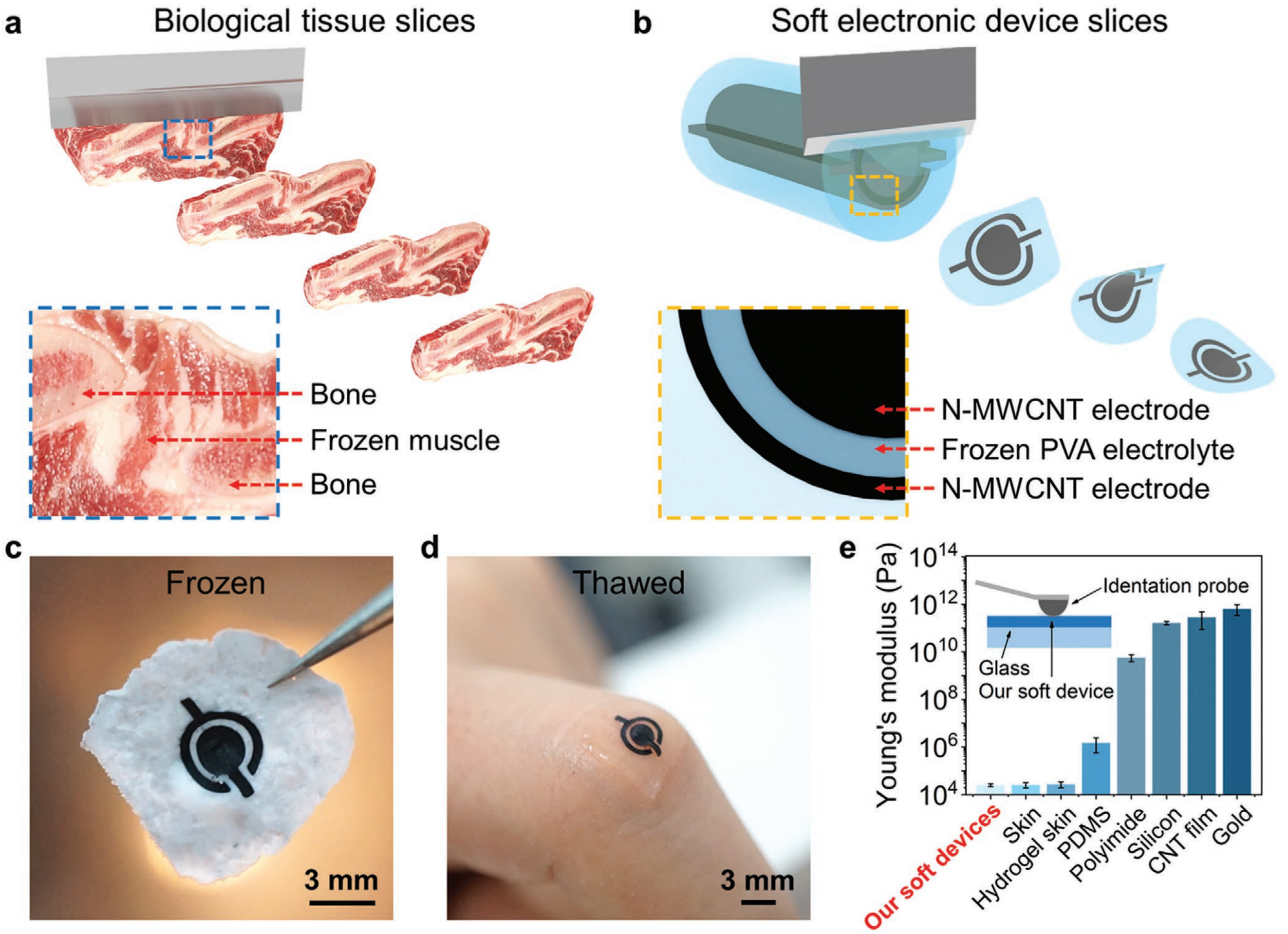

Figure 1. Soft electronic devices inspired by the fabrication technique of multicomponent biological tissue slices. a,b) Schematic sketch of the fabrication process of a) multicomponent biological tissue slices and b) soft electronic device slices via cryo-microtomy. c,d) A freshly prepared electronic device slice in frozen and thawed state, respectively. e) Comparison of Young's modulus values among our soft electronic device slices, skin, and other commonly used materials in skin-mounted or implantable electronic devices (inset, schematic diagram of test equipment).

at high speeds of above 20 devices per minute for one slicing slot even at lab. Besides, the supercapacitors showed a low average effective Young's modulus of 25.2 kPa, near to that of fresh skin (25.3 kPa), realizing a conformal contact with skin (Figure 1d,e; Figure S2, and Table S1, Supporting Information). This hydrogel cryo-microtomy was further extended to prepare soft sensors which detected strain, pressure, and temperature successfully.

2. Results and Discussion

2.1. Penetration of Low-Modulus Aqueous PVA Electrolyte into High-Modulus Aligned N-MWCNT Array Electrodes

To realize uniform modulus during sectioning, on the one hand, PVA electrolyte, such as PVA-phosphoric acid (H_3PO_4) electrolyte, should penetrate sufficiently into the N-MWCNT electrodes without causing damages. The realization of interpenetrated network can also help to pass on the mechanical properties of PVA electrolyte well to the whole device. On the other hand, the modulus of PVA electrolyte should be raised to a higher value compatible with that of N-MWCNT electrodes to narrow the modulus gap. Here, the vertically porous channels of aligned N-MWCNT array electrode allowed for the downward penetration of sol-state PVA electrolyte along the alignment direction (**Figure 2**).[13,14] It should be noted that pristine aligned MWCNT array could not maintain customized patterns during the penetration process, due to the generated deflection of MWCNTs caused by the capillary force of solvent.[15,16] However, aligned N-MWCNT arrays were relieved from the trouble as their diameters were much bigger than the former owing to the regrown nitrogen-doped graphitized carbon layer on the MWCNTs (Figure S3, Supporting Information). Specifically, with the extension of regrowth period, the outer diameter increased from 11 nm for single MWCNT to 23 nm for single N-MWCNT-10 min (regrowth period of 10 min), and 44 nm for single N-MWCNT-20 min (regrowth period of 20 min) (Figure S3a–c, Supporting Information). In spite of the increased diameters, aligned N-MWCNT arrays were still loose enough for the penetration of PVA electrolyte (Figure S3d–i, Supporting Information). The maximum

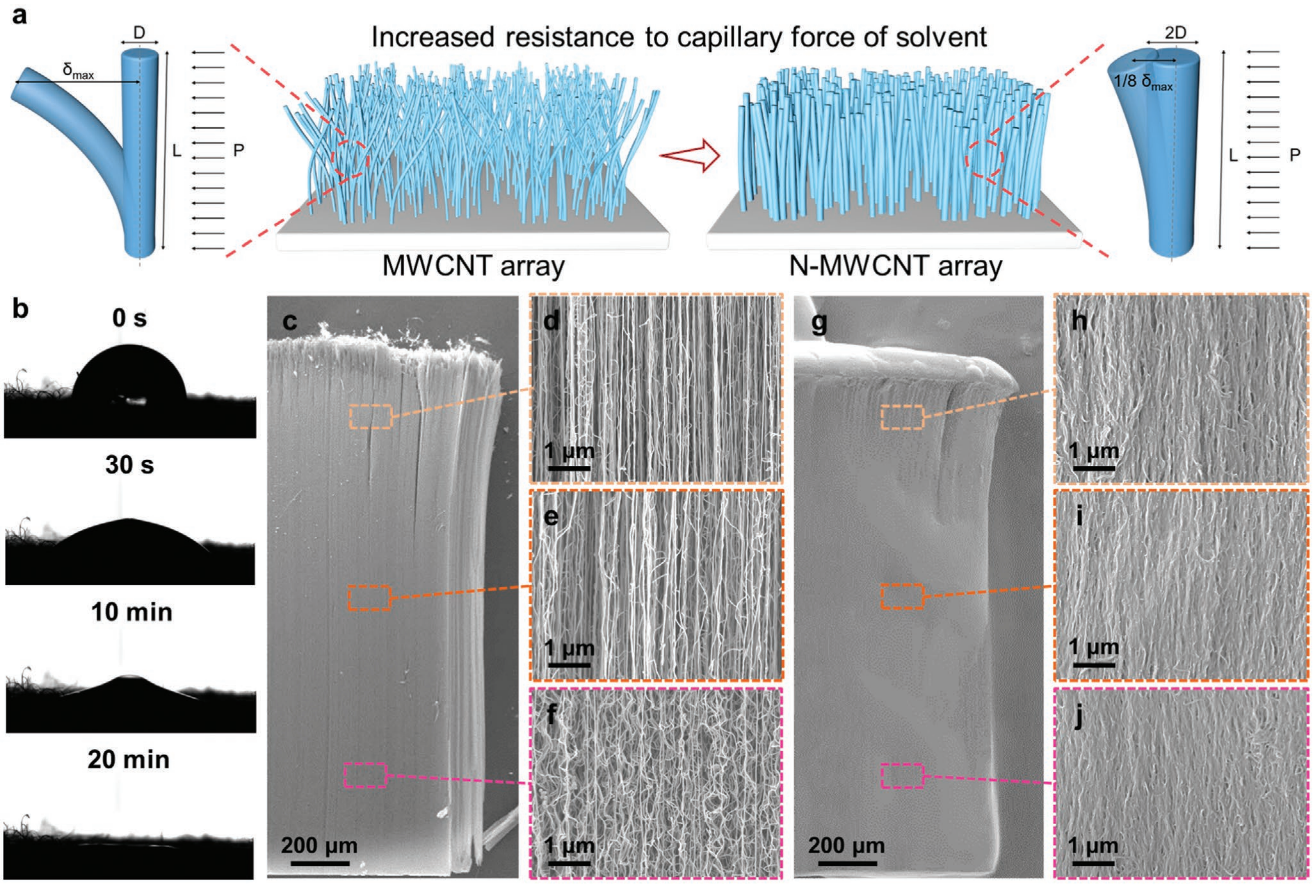

Figure 2. Penetration of low-modulus aqueous PVA electrolyte into high-modulus aligned N-MWCNT array electrodes. a) Schematic diagram to the effect of capillary force of water on the deflection of MWCNT and N-MWCNT. b) Optical microscopic images for a drop of 10 µL PVA electrolyte containing 0.06 g mL^{-1} PVA and 1.0 м H_3PO_4 penetrating into the N-MWCNT electrode. c–j) Scanning electron microscopy images of the side surface and corresponding enlarged views at different heights along the alignment direction of N-MWCNT array before (c–f) and after (g–j) the penetration of PVA electrolyte containing 0.09 g mL^{-1} PVA and 1.0 м H_3PO_4.

deflection for N-MWCNT-10 min decreased to one eighth of the value for MWCNT under the same solvent pressure (Figure 2a, details of calculation of maximum deflection presented in Supporting Information). N-MWCNTs also showed more defect sites and disorders (Figure S4, Supporting Information), and a slightly improved hydrophilicity facilitating the penetration of aqueous PVA electrolyte (Figure S5, Supporting Information), due to the doped nitrogen atoms which mainly presented in the forms of quaternary-N (401.91 eV) and N-oxide of pyridinic-N (403.53 eV) (Figure S6, Supporting Information).[17,18] To ensure the structural stability, regrowth period of 10 min was used later if not specified, as N-MWCNT array with longer regrowth period tended to collapse during the regrowth process (Figure S7, Supporting Information).

Besides, PVA electrolyte should have good fluidity to fully penetrate into N-MWCNT array electrodes. A drop of 10 µL sol-state PVA electrolyte composed of 0.06 g mL^{-1} PVA and 1.0 м H_3PO_4 completely penetrated into the gap among N-MWCNT bundles in 20 min (Figure 2b). The PVA concentration had a strong effect on the penetration process of PVA electrolyte into N-MWCNT arrays. A higher PVA concentration realized a higher gelation density but caused a higher viscosity which hindered the penetration of PVA electrolyte. H_3PO_4 solution without PVA completely penetrated into N-MWCNT array quickly (10 µL of solution completed in 16 s, Figure S8a, Supporting Information). Nevertheless, the total time needed for 10 µL of PVA electrolyte completely penetrating into N-MWCNT electrodes ascended from 9 to 20, 47, and 57 min with the increasing PVA concentration from 0.03 to 0.06, 0.09, and 0.12 g mL^{-1} (Figure S8b–e, Supporting Information). Corresponding rheological analysis showed that the viscosities of sol-state PVA electrolyte increased distinctly from 9.0 to 540.1 mPa·s as the PVA concentration went up from 0.03 to 0.09 g mL^{-1}, which then increased to 1297.8 mPa·s as the PVA concentration further rose to 0.12 g mL^{-1} (Figure S9a, Supporting Information). Besides, the ion conductivities of the sol and gel counterparts demonstrated little dependence on the PVA concentration from 0.03 to 0.12 g mL^{-1} (Figure S9b, Supporting Information). Hence, 0.09 g mL^{-1} PVA was used in the following work to balance high gelation density and short penetration time. After the penetration in massive PVA electrolyte followed by a 12-hour standing process, N-MWCNT array electrodes were fully penetrated by PVA electrolyte, achieving an interpenetrated network from top to bottom (Figure 2c–j).

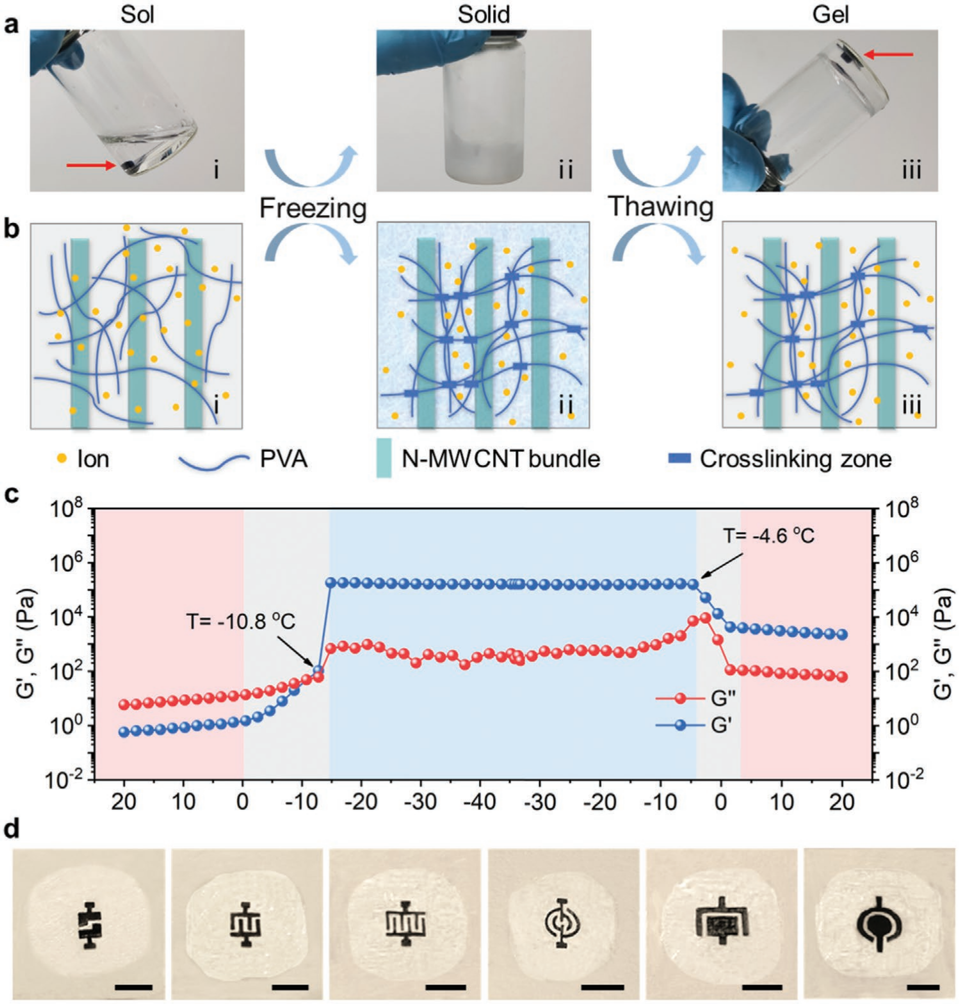

Figure 3. A sol-solid-gel transition of interpenetrated network comprising PVA electrolyte and N-MWCNT array electrodes during the freeze-thaw process. a,b) Photographs and schematic illustration of the freeze-thaw process of the aligned N-MWCNT array electrodes penetrated by PVA electrolyte, respectively. The red arrows in (a) indicate the aligned N-MWCNT array electrodes. c) Change of G' and G'' of PVA electrolyte comprising 0.09 g mL^{-1} PVA and 1.0 M H_3PO_4 versus temperature during the freeze-thaw process. d) Photographs of soft electronic device slices at the gel state with different patterns. All the scale bars in (d), 3 mm.

2.2. A Sol-Solid-Gel Transition of Interpenetrated Network Comprising PVA Electrolyte and N-MWCNT Array Electrodes

PVA electrolyte penetrated into N-MWCNT array electrodes like a liquid at the sol state, underwent a spontaneous crosslinking process when freezing, and then supported device structure like a quasi-solid after thawing into gel state, i.e., a sol-solid-gel transition (**Figure 3**a,b). At the sol state, free PVA chains distributed randomly in the gap among N-MWCNT bundles (Figure 3bi). Standing at about –30 °C for several minutes, the water in the PVA electrolyte froze and expanded, forcing PVA chains to aggregate and orient and then facilitating the formation of crystallites and hydrogen bonds, both of which acted as crosslinking points of PVA hydrogel (Figure 3bii).[19–21] Many crosslinking points remained after thawing, yielding a hydrogel crosslinking network in the resulting quasi-solid-state soft electronic devices (Figure 3biii). The measured dynamic storage (G') and loss (G'') shear modulus of PVA electrolyte in the cooling (from 20 to –40 °C) and heating (from –40 to 20 °C) process supported this sol-solid-gel transition (Figure 3c). During the cooling process, G' increased and overtook G'' at about –10.8 °C, referring to a transition from sol to solid.[22] In this sol to solid process, G' of PVA electrolyte significantly increased by over five orders of magnitude to above 10^5 Pa, and the modulus mismatch between PVA electrolyte and N-MWCNT electrode was significantly alleviated, which was beneficial to construct stable interfaces between these components. As to the heating process, G' kept surpassing G'' although the temperature reached and exceeded phase transition temperature of about –4.6 °C, indicating a transition from solid- to quasi-solid-state gel. And G' of gel-state PVA electrolyte was three orders of magnitude higher than that of sol-state PVA electrolyte but two orders of magnitude lower than that of solid-state counterpart. The higher phase transition temperature during heating process might originate from the presence of crosslinked PVA hydrogel network and the endothermic process of ice melting. Furthermore, X-ray diffraction analysis confirmed the formation of crystallites after thawing (Figure S10, Supporting Information). Specifically, pristine commercial PVA plastic pieces showed the primary crystalline peak at 19.4° as reported.[19] Dissolving PVA plastic pieces for preparing PVA electrolyte broke the crystalline structure, causing the disappearance of crystalline peak. However, freeze-thawed PVA electrolyte showed a weak crystalline peak indicating the crystalline remodeling to some extent. To further improve structural and mechanical stability, additional freeze-thaw cycles and/or chemical crosslinking reagents (e.g., borax) can be adopted.

According to Figure 3c, the phase transition temperature of PVA-H_3PO_4 electrolyte deviated from the theoretical freezing point of water. It mainly resulted from the existence of H_3PO_4 which obviously lowered the phase transition temperature of water related to the colligative properties of solutions (Figure S11, Supporting Information). Hence, H_3PO_4 concentration was further investigated. The freezing point of PVA-H_3PO_4 electrolyte decreased as H_3PO_4 concentration rose (Figure S12a, Supporting Information), which meant more liquid nitrogen was needed to lower the temperature for freezing the PVA-H_3PO_4 electrolyte with higher H_3PO_4 concentration. On the other hand, higher H_3PO_4 concentration was able to enhance the ion conductivity of PVA-H_3PO_4 electrolyte which increased from 34 to 86 mS cm^{-1} with H_3PO_4 concentration increasing from 0.5 to 2.0 M no matter whether PVA-H_3PO_4 electrolyte was at the sol or gel state (Figure S12b, Supporting Information). To balance the energy consumption and ion conductivity, 1.0 M H_3PO_4 was used in the PVA-H_3PO_4 electrolyte if not specified. Even so, higher-concentration PVA-H_3PO_4 electrolyte can still be used under lower temperatures if higher ion conductivities are required.

2.3. Soft Supercapacitors Fabricated by Hydrogel Cryo-Microtomy

Based on the PVA-H_3PO_4 electrolyte (consisting of 0.09 g mL^{-1} PVA and 1.0 M H_3PO_4) and N-MWCNT array electrodes, soft supercapacitors with controllable electrode structures were fabricated via cryo-microtomy. The electrode structure (i.e., N-MWCNT array pattern) was easily designed by using different delicate masks such as interdigital, circle, and rectangle (Figure 3d and Figure S13, Supporting Information). Generally, the electrode structure had an impact on the electrochemical performances of resulting devices.[23–25] Therefore, typical interdigital electrodes with different finger numbers were prepared and investigated. Clearly, the soft supercapacitors based on 3-finger interdigitated pattern demonstrated higher charge-storage capacity and higher energy density at high power density (Figure S14, Supporting Information). It was because that the supercapacitors of 3-finger interdigitated pattern provided more surface accessible to electrolyte ions and lower equivalent series resistance than the counterparts of 2-finger and 1-finger with the same electrode geometric area. Hence, soft supercapacitors with 3-finger interdigitated pattern were adopted in the following experiments if not specified.

What highlights the hydrogel cryo-microtomy is the easy controllability of device thickness. Soft supercapacitors with desired thickness were able to be realized by simply adjusting the feed distance of microtome, ranging from 0.5 to 600 µm. Typical cross-sectional images of electrodes with different thicknesses are showed in **Figure 4**a–c. Relationship of electrochemical performances with device thickness was further studied. All the soft supercapacitors presented triangular galvanostatic charge-discharge curves (Figure 4d) and rectangle cyclic voltammetry curves (Figure S15 Supporting Information). Specifically, the areal capacitance of supercapacitors increased from 0.56 to 9.42 mF cm^{-2} as device thickness augmented from 5 to 90 µm (Figure 4e). Basically, the device performances showed an almost linear dependence on thickness, and we therefore were able to choose thicker supercapacitors towards higher energy demand. Typical cyclic voltammetry and galvanostatic charge-discharge curves were presented in Figure 4f and Figure S16, Supporting Information, for a soft supercapacitor with thickness of 50 µm, respectively.

In addition to the above-mentioned controllable pattern and device thickness, the hydrogel cryo-microtomy method endows the as-prepared devices with high yield. Dozens of soft supercapacitors were able to be prepared in minutes depending on the chosen sectioning speed of microtome. For instance, 100 soft supercapacitors with a thickness of 10 µm were prepared in 5 min by the lab-level equipment (i.e., microtome) at a speed of about 3 s stroke^{-1} (or 5 mm s^{-1}). The yield is expected to be significantly improved to 7500 devices in 5 min through a larger-scale equipment (Figure S17, Supporting Information). Figure 4g depicts 48 soft supercapacitors with shared parameters including the electrode pattern (3-finger interdigital pattern), device thickness (50 µm), and sectioning speed (3 s stroke^{-1} or 5 mm s^{-1}). Further statistical analysis on the performances of 30 supercapacitors showed that the cryo-microtomy achieved high reproducibility with device areal capacitances of over 75% devices distributed in the range of 15% fluctuation (Figure 4h). Further, the resulting supercapacitors showed good cyclic performance with initial capacitance retention at 92.4% after 10 000 cycles of charge and discharge (Figure 4i). The coulombic efficiency ranged from 92 to 100% during these charge-discharge cycles, and a value of 91.8% was maintained after 10 000 cycles (Figure S18, Supporting Information). Meanwhile, the supercapacitor, taking the circle electrode pattern as an example, succeeded in adapting to the deformation without a significant performance degradation, when it was compressed and stretched as the knuckle extended and bended, respectively (Figure 4j). For the purpose of practical applications, supercapacitors in series and parallel were exercised to extend the voltage window and discharge time, respectively (Figure 4k,l).

Another advantage of using cryo-microtomy to prepare soft supercapacitors lies in the designability of electrolyte components to meet specific needs, such as biocompatibility or higher electrochemical performance. For the safety of supercapacitors on the skin or even in vivo, H_3PO_4 solution was replaced by saline or phosphate buffered saline (PBS) and such low-concentration electrolytes still worked in the supercapacitors (Figure S19, Supporting Information). Soluble redox species of potassium iodide (KI) and vanadium sulfate ($VOSO_4$) were also added to the pristine PVA-H_3PO_4 gel electrolyte to improve the specific capacitance and energy density of supercapacitors (Figure S20, Supporting Information), as demonstrated in the literature.[26,27] The device areal capacitance increased

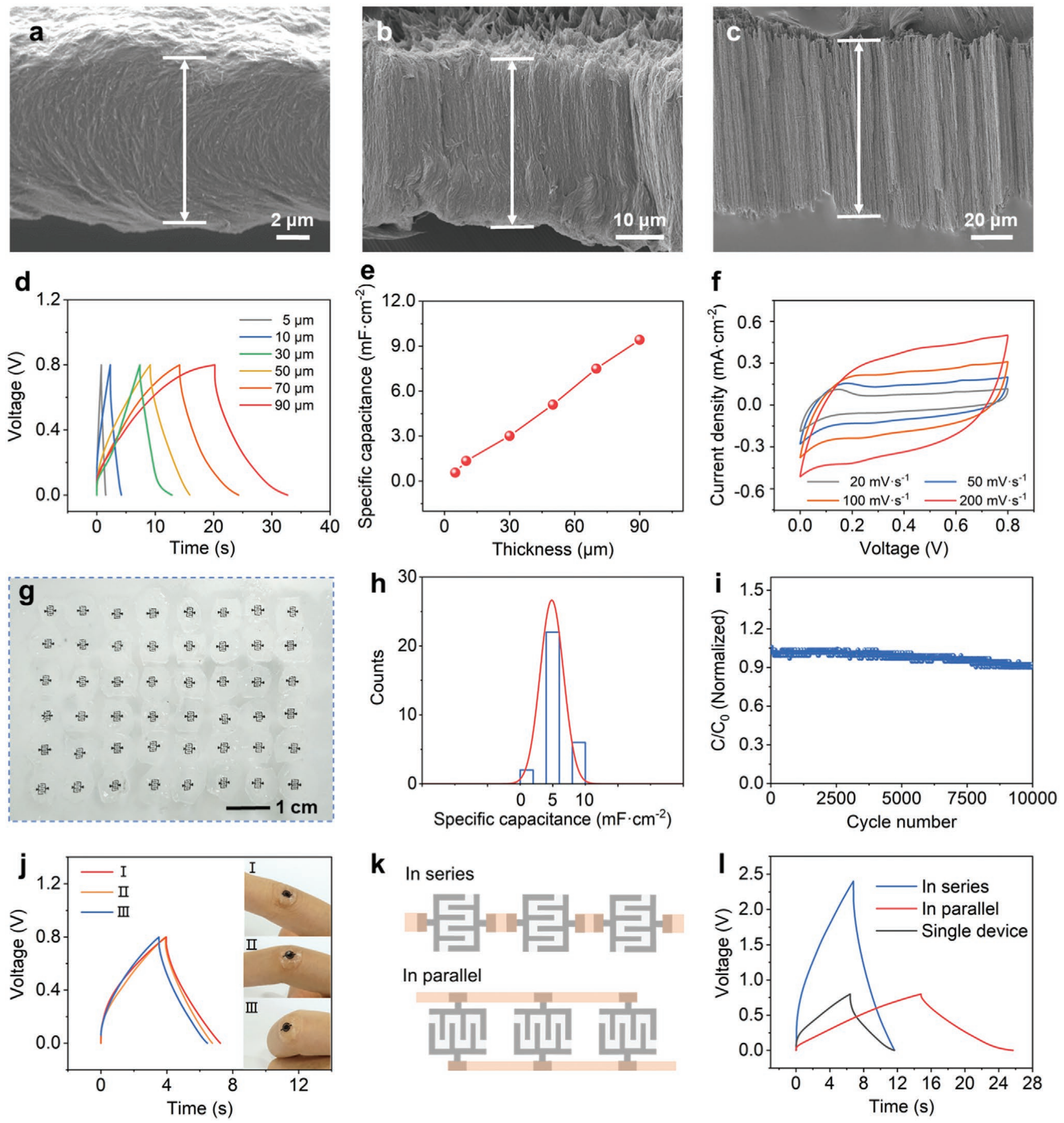

Figure 4. Soft supercapacitors fabricated by hydrogel cryo-microtomy. a–c) Cross-sectional scanning electron microscopy images of N-MWCNT electrodes derived from soft supercapacitors sectioned at thicknesses of 10, 30, and 90 μm, respectively. d) Galvanostatic charge-discharge curves for supercapacitors with thickness range from 5 to 90 μm at 0.6 mA cm^{-2}. e) Dependence of areal capacitance on device thickness. f) Typical cyclic voltammograms for the supercapacitor with thickness of 50 μm at different scan rates. g) Photograph for 48 supercapacitors with shared parameters. h) Histogram of areal capacitances of 30 supercapacitors fabricated with the same parameters. i) Cyclic performance of the supercapacitor with thickness of 50 μm. C$_0$ and C referred to the capacitance before and after cycling, respectively. j) Galvanostatic charge-discharge curves of the supercapacitor with thickness of 50 μm at compressing (I), original (II), and stretching (III) states on the knuckle of a finger (insert, corresponding photographs). k,l) Schematic and galvanostatic charge-discharge curves of supercapacitors measured in single, series, and parallel, respectively.

from 7.3 mF cm^{-2} based on pristine electrolyte (Figure S16, Supporting Information) to 23.1 mF cm^{-2} based on modified electrolyte (Figure S20b, Supporting Information), much higher than many recently reported advanced supercapacitors (Table S2, Supporting Information)[28–34]. Furthermore, the modified device delivered a high areal energy density of

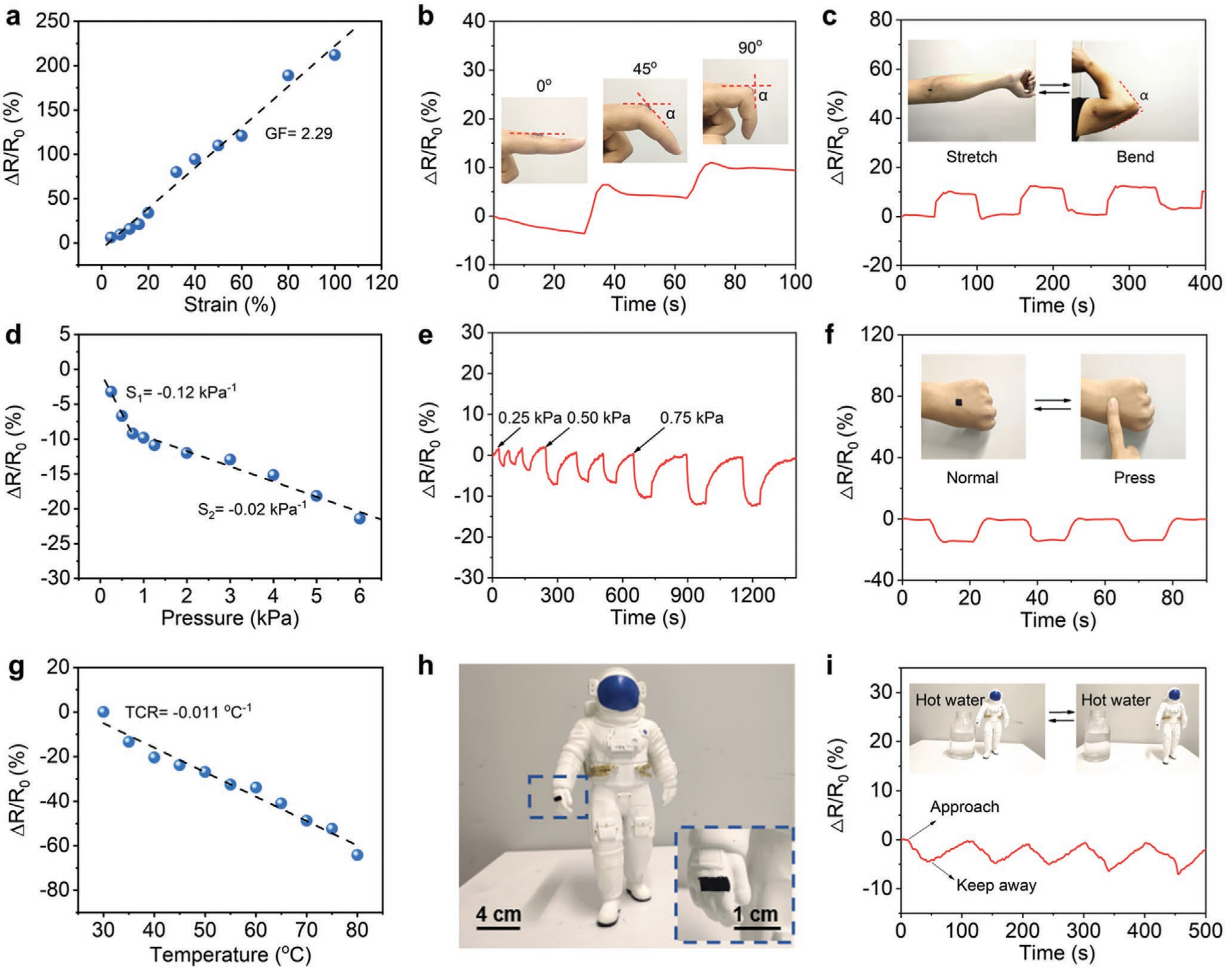

Figure 5. Soft sensors fabricated by hydrogel cryo-microtomy. a) Relative resistance changes versus strain for the strain sensor. b,c) Relative resistance changes of the strain sensor attached to b) a human finger under different bending angles and c) a human elbow under repeatable stretching/bending cycles. d) Relative resistance changes versus pressure for the pressure sensor. e,f) Relative resistance changes of the pressure sensor e) under pressures of 0.25, 0.50, and 0.75 kPa repeatedly and f) attached to a human hand under repeatable pressing/releasing cycles. g) Relative resistance changes versus temperature for the temperature sensor. h) Photographs of a temperature sensor attached to an astronaut model. i) Relative resistance changes of the temperature sensor on the astronaut model when a bottle of hot water of approximately 70 °C approached/kept away repeatedly. R_0 and ΔR refer to initial resistance and resistance change with measuring, respectively. The sensors used here were 500 µm in thickness.

8.20 µWh cm^{-2} and power density of 2400 µW cm^{-2}, respectively, comparable with the reported state-of-the-art supercapacitors (Table S3, Supporting Information).[28–30,35]

2.4. Soft Sensors Fabricated by Hydrogel Cryo-Microtomy

Furthermore, this cryo-microtomy method was able to be extended to fabricate other kinds of soft electronic devices based on conductive nanomaterials beyond aligned N-MWCNT arrays. As a demonstration, soft sensors were fabricated using the composites of carboxylic acid functionalized MWCNTs and bare PVA sol. After the same cryo-microtomy process as soft supercapacitor slices, the soft sensors were chemically crosslinked by borax further. The obtained sensors encapsulated by parafilm succeeded in response to strain, pressure, and temperature, since the carriers hopping changed with applied stimuli (Figure S21, Supporting Information). The thickness of sensors had an impact on the sensitivity. A thicker sensor had a higher sensitivity with a higher gauge factor (GF) taking strain sensor as an example (Figure S22, Supporting Information). It was because that a thicker sensor had a lower initial resistance. Hence, a thickness of 500 µm was chosen for further research. Systematic characterization of the strain sensor on the strain range from 4 to 100% was carried out, which showed a GF of 2.29 ($R^2 = 0.98$) (**Figure 5**a). Based on the strain sensor, human motions including finger and elbow bending were detected successfully (Figure 5b,c). When this sensor acted as a pressure sensor, it responded to pressures from 0.25 to 0.75 kPa with a sensitivity of −0.12 kPa^{-1} (S_1, $R^2 = 0.99$) and pressures from 1 to 6 kPa with a sensitivity of −0.02 kPa^{-1} (S_2, $R^2 = 0.97$) (Figure 5d). Moreover, the pressure sensor successfully monitored the applied pressures when it was attached onto a hand (Figure 5e,f). In addition to strain and pressure, this sensor was sensible to temperature variation. The resistance of sensor decreased with increasing temperatures with a negative thermosensitive feature where carriers hopping accelerated and the desorption of water molecules further reduced the spacing among MWCNTs under increased temperatures.[36,37] This temperature sensor showed a linear response with a temperature coefficient of resistance of –0.011 °C^{-1} ($R^2 = 0.97$) in a temperature range from 30 to 80 °C (Figure 5g). Further the temperature sensor was developed as soft electronic skin (Figure 5h), endowing an astronaut model with the capability to perceive the approaching and withdrawing of heat source (Figure 5i).

3. Conclusion

In conclusion, inspired by the freeze-section process of multicomponent biological tissues with low modulus muscles and high-modulus bones, we have proposed a hydrogel cryo-microtomy method to fabricate soft electronic devices with high-modulus N-MWCNT electrodes and low-modulus PVA electrolyte. Specifically, stable interfaces formed between N-MWCNT electrodes and frozen PVA electrolyte at subzero temperature due to the significantly increased modulus of frozen PVA electrolyte. Then dozens of soft supercapacitors (effective Young's modulus of 25.2 kPa close to the value of skin) were constructed with controllable pattern, tunable thickness from 0.5 to 600 µm, high yield (100 devices in 5 min even at lab scale) and high reproducibility (over 75% devices with 15% performance fluctuation). Soft sensors were further fabricated using carboxylic acid functionalized MWCNTs and bare PVA sol, which were able to detect strain, pressure, and temperature. This cryo-microtomy method can be generalized to prepare more kinds of soft electronic devices with high controllability, yield, and reproductivity towards wearable and implantable applications.

4. Experimental Section

Reagents: PVA (1750, Sinopharm Chemical Reagent), H_3PO_4 (85 wt%, Aladdin), $VOSO_4$ (99.9%, Alfa), KI (99.9%, Adamas), acetonitrile (99.9%, Aladdin), carboxylic acid functionalized multiwalled carbon nanotubes (MWCNTs) (99%, Chengdu Organic Chemicals Co. Ltd.), sodium dodecyl benzene sulfonate (99.9%, Sinopharm Chemical Reagent), and sodium tetraborate (borax, 99.9%, Adamas) were used as received without further purification. PBS (0.01 м, containing Na_2HPO_4, KH_2PO_4, NaCl, and KCl) was purchased from Solarbio Science and Technology Co. Ltd. Saline (0.9 wt% sodium chloride) was obtained from Shijiazhuang No.4 Pharmaceutical Co. Ltd.

Preparation of Patterned Aligned Nitrogen-Doped Multi-Walled Carbon Nanotube (N-MWCNT) Arrays: First, a series of patterns were designed using AutoCAD software and then processed on a stainless-steel mask with a diameter of 4 inches by chemical etching (Shenzhen Weina Technology Co. Ltd., with an accuracy of ±15 µm). Second, the patterned catalyst (5 nm Al_2O_3, 1.2 nm Fe) was deposited on the silicon wafer of 4 inches under the cover of customized mask by vacuum electron beam evaporation. Next, patterned aligned MWCNT arrays were synthesized through chemical vapor deposition at 740 °C for 90 min in a tube furnace, with ethylene (flowing rate of 30 sccm) as the carbon precursor and a mixture of argon (flowing rate of 400 sccm) and H_2 (flowing rate of 90 sccm) as the carrier gas.[38] The typical height of MWCNT arrays was around 1.5 mm. Finally, the above MWCNT arrays were transferred to another high-temperature tube furnace. Aligned N-MWCNT arrays were prepared at 1060 °C within 10–20 min with acetonitrile as both carbon and nitrogen source which was carried into the quartz tube by argon (flowing rate of 30 sccm), and a mixture gas of hydrogen (flowing rate of 10 sccm) and argon (flowing rate of 110 sccm) served as carrier gas.[39]

Fabrication of Soft Supercapacitors by Cryo-Microtomy: Typically, aqueous PVA-H_3PO_4 sol electrolyte was used as the embedding materials for aligned N-MWCNT array electrodes. It was prepared by dissolving 0.3–1.2 g PVA in 10 mL of deionized water at 90 °C for 2 h, followed by introduction of H_3PO_4 to prepare 0.5–2.0 м H_3PO_4. The freshly prepared sol electrolyte in low viscosity was instantly cast into a N-MWCNT array in a stainless-steel container at 90 °C, which was then sealed by the parafilm to inhibit the water evaporation loss and stood for 12 h at least to facilitate the penetration of sol electrolyte into the N-MWCNT array. The resulting sol-soaked array was removed from the container and placed vertically upward in a stainless-steel sample pool of the freezing chamber (Leica LN 22) of microtome (Leica RM 2265). Liquid nitrogen was used to maintain the temperature of the freezing chamber at around –30 °C. After the sol electrolyte in the N-MWCNT array was completely frozen, the sample pool was rotated by 90 ° and fixed on the sample holder. A tungsten carbide blade (Leica, Klinge, 30 mm, 40°, 25693) was used to section the frozen sol-soaked array perpendicularly to the N-MWCNT alignment direction to prepare frozen solid supercapacitors. Then soft supercapacitors were obtained after a natural thawing process. The thickness of supercapacitors was able to be controlled by adjusting the feed distance (0.5–600 µm) of the microtome. PBS-based and saline-based supercapacitors were prepared by replacing the H_3PO_4 solution with PBS and saline solution during the immersing stage. Besides, redox mediators modified supercapacitors were obtained by soaking the pristine supercapacitors in the corresponding redox electrolytes such as KI and $VOSO_4$ solutions.

Preparation of Soft Sensors by Cryo-Microtomy: 50 mg carboxylic acid functionalized MWCNTs and 50 mg sodium dodecyl benzene sulfonate were uniformly dispersed into 5 mL of deionized water using ultrasonic cell pulverizer (JY88-IIN, Ningbo Xinzhi Biotechnology Co. Ltd.) for 6 h to ensure a complete dispersion of MWCNTs. Then, 5 mL 0.09 g mL^{-1} PVA sol was added to the above dispersion and the mixture was further dispersed under sonication. Similar to the preparation process of soft supercapacitor slices, the above mixture was frozen and sectioned in an environment of about –30 °C to obtain slices with different thicknesses (100, 200, and 500 µm). After a natural thawing process, the slices were immersed in a 4 wt% borax solution for 1 min to obtain the free-standing chemically crosslinked soft sensor. The size of the soft sensor used for strain, pressure, and temperature sensing tests were 0.5 × 1, 1 × 1, and 0.5 × 1 cm^2, respectively. Copper foil was used to draw test leads from both ends of the sensor. Parafilm was used to encapsulate the sensor to prevent the evaporation loss of water in the hydrogel during tests. For the strain/pressure sensing tests, the sensors were fixed on home-built devices to apply different strains/pressures. For the temperature sensing tests, a high-temperature hot stage was used to provide a temperature range of 30–80 °C. Before the tests, the temperature sensor was kept at different temperatures for 15 min to ensure the reliability of the test results.

Testing and Characterization: The electrochemical measurements were performed on an electrochemical workstation (CHI 660E, Shanghai Chenhua Ltd). The cyclic performance was characterized at the Arbin electrochemical testing system (MSTAT-5 V/10 mA/16 Ch). The morphology and structure of MWCNT and N-MWCNT were characterized by field-emission scanning electron microscopy (Zeiss ultra-55, operated at 5 kV, gold particles were deposited on the sample surface at 10 mA for 60 s), transmission electron microscopy (JEOL, JEM-2100F operated at 200 kV), Raman spectroscopy (HORIBA JobinYvon XploRA, with an excitation wavelength of 532 nm and laser power of 100 mW) and X-ray photoelectron spectroscopy (PHI 5000C&PHI5300, Mg, 250 W, 14 kV). The crystallinity of PVA samples was analyzed using X-ray diffraction spectrometer (D8 ADVANCE).

Dynamic storage (G') and loss (G'') shear modulus and viscosities of PVA electrolyte were measured on the rotational rheometer (HAAKE MARS III). Based on the oscillation temperature steps mode, with a fixed strain of 0.1% and frequency of 1 Hz, G' and G'' of PVA electrolyte at different temperatures were recorded when the temperatures became stable every 1 °C (the temperature was reduced from 25 to –40 °C at a rate of 2 °C min^{-1} and remained at –40 °C for 30 min, followed by increase back to 25 °C). The viscosities were tested by controlling the angular velocity scanning from 10 to 0.1 rad s^{-1} at 25 °C based on the Steady State Rotation mode. The freezing points of electrolyte, PVA sol, and deionized water were obtained on differential scanning calorimetry (TA Q2000). A sample of 10 mg was placed in a pre-weighed aluminum sample pan with a TA sealing press, with another identical pre-weighed sealed aluminum pan as the reference pan. The sealed pans were firstly cooled down to –60 °C at the rate of 10 °C min^{-1}, then equilibrated at –60 °C for 10 min, followed by a heating-up step from –60 to 20 °C at a rate of 5 °C min^{-1}.[40] Photographs were taken using a digital camera (Nikon, J1). Effective Young's moduli of slices and skin samples were characterized in a Piuma Nanoindenter (Optics 11 BV) equipped with a spherical indenter of 0.48 N m^{-1} in stiffness and 10 µm in diameter. Due to the unavailability of human skin samples, a piece of fresh pig skin was used for testing. Effective Young's moduli of materials were calculated from the unloading part of the curves according to the Hertz model.

The experiments concerned with fresh pig skin, finger, hand and arm of human were approved by Animal and Human Experimentation Committee of Fudan University. A healthy subject from Fudan University was gave written, informed consent before participating in the study.

Supporting Information

Supporting Information is available from the Wiley Online Library or from the author.

Acknowledgements

X.F. and J.L. contributed equally to this work. This work was supported by MOST (2016YFA0203302), NSFC (21634003, 21604012, and 51673043), STCSM (18QA1400700), SHMEC (2017-01-07-00-07-E00062), and Yanchang Petroleum Group.

Conflict of Interest

The authors declare no conflict of interest.

Keywords

cryo-microtomy, hydrogel, sensor, soft electronics, supercapacitor

Received: September 30, 2020
Revised: October 30, 2020

---

[1] H. U. Chung, B. H. Kim, J. Y. Lee, J. Lee, Z. Xie, E. M. Ibler, K. Lee, A. Banks, J. Y. Jeong, J. Kim, C. Ogle, D. Grande, Y. Yu, H. Jang, P. Assem, D. Ryu, J. W. Kwak, M. Namkoong, J. Bin Park, Y. Lee, D. H. Kim, A. Ryu, J. Jeong, K. You, B. Ji, Z. Liu, Q. Huo, X. Feng, Y. Deng, Y. Xu, et al., *Science* **2019**, *363*, eaau0780.

[2] X. Chen, Lu Yin, J. Lv, A. J. Gross, M. Le, N. G. Gutierrez, Y. Li, I. Jeerapan, F. Giroud, A. Berezovska, R. K. O'Reilly, S. Xu, S. Cosnier, J. Wang, *Adv. Funct. Mater.* **2019**, *29*, 1905785.

[3] W. Gao, S. Emaminejad, H. Y. Y. Nyein, S. Challa, K. Chen, A. Peck, H. M. Fahad, H. Ota, H. Shiraki, D. Kiriya, D. H. Lien, G. A. Brooks, R. W. Davis, A. Javey, *Nature* **2016**, *529*, 509.

[4] B. Wang, X. Fang, H. Sun, S. He, J. Ren, Y. Zhang, H. Peng, *Adv. Mater.* **2015**, *27*, 7854.

[5] L. Wang, S. Xie, Z. Wang, F. Liu, Y. Yang, C. Tang, X. Wu, P. Liu, Y. Li, H. Saiyin, S. Zheng, X. Sun, F. Xu, H. Yu, H. Peng, *Nat. Biomed. Eng.* **2020**, *4*, 159.

[6] K. Yamagishi, I. Kirino, I. Takahashi, H. Amano, S. Takeoka, Y. Morimoto, T. Fujie, *Nat. Biomed. Eng.* **2019**, *3*, 27.

[7] Y. Wang, S. Lee, T. Yokota, H. Wang, Z. Jiang, J. Wang, M. Koizumi, T. Someya, *Sci. Adv.* **2020**, *6*, eabb7043.

[8] Z. Liu, Z. S. Wu, S. Yang, R. Dong, X. Feng, K. Müllen, *Adv. Mater.* **2016**, *28*, 2217.

[9] L. Lipani, B. G. R. Dupont, F. Doungmene, F. Marken, R. M. Tyrrell, R. H. Guy, A. Ilie, *Nat. Nanotechnol.* **2018**, *13*, 504.

[10] H. Zhang, W. Han, K. Xu, Y. Zhang, Y. Lu, Z. Nie, Y. Du, J. Zhu, W. Huang, *Nano Lett.* **2020**, *20*, 3449.

[11] H. Li, T. Lv, H. Sun, G. Qian, N. Li, Y. Yao, T. Chen, *Nat. Commun.* **2019**, *10*, 536.

[12] T. Lv, Y. Yao, N. Li, T. Chen, *Angew. Chem., Int. Ed.* **2016**, *55*, 9191.

[13] S. He, L. Qiu, L. Wang, J. Cao, S. Xie, Q. Gao, Z. Zhang, J. Zhang, B. Wang, H. Peng, *J. Mater. Chem. A* **2016**, *4*, 14968.

[14] K. Liu, Y. Yao, T. Lv, H. Li, N. Li, Z. Chen, G. Qian, T. Chen, *J. Power Sources* **2020**, *446*, 227355.

[15] D. N. Futaba, K. Hata, T. Yamada, T. Hiraoka, Y. Hayamizu, Y. Kakudate, O. Tanaike, H. Hatori, M. Yumura, S. Iijima, *Nat. Mater.* **2006**, *5*, 987.

[16] H. Liu, S. Li, J. Zhai, H. Li, Q. Zheng, L. Jiang, D. Zhu, *Angew. Chem., Int. Ed.* **2004**, *43*, 1146.

[17] Z. Zhang, L. Wang, Y. Li, Y. Wang, J. Zhang, G. Guan, Z. Pan, G. Zheng, H. Peng, *Adv. Energy Mater.* **2017**, *7*, 1601814.

[18] K. S. Lee, W. J. Lee, N.-G. Park, S. O. Kim, J. H. Park, *Chem. Commun.* **2011**, *47*, 4264.

[19] J. L. Holloway, A. M. Lowman, G. R. Palmese, *Soft Matter* **2013**, *9*, 826.

[20] H. Zhang, F. Zhang, J. Wu, *React. Funct. Polym.* **2013**, *73*, 923.

[21] T. Hatakeyema, J. Uno, C. Yamada, A. Kishi, H. Hatakeyama, *Thermochim. Acta* **2005**, *431*, 144.

[22] Q. Zhao, X. Liu, S. Stalin, K. Khan, L. A. Archer, *Nat. Energy* **2019**, *4*, 365.

[23] S. Wang, Z. S. Wu, S. Zheng, F. Zhou, C. Sun, H. M. Cheng, X. Bao, *ACS Nano* **2017**, *11*, 4283.

[24] S. He, J. Cao, S. Xie, J. Deng, Q. Gao, L. Qiu, J. Zhang, L. Wang, Y. Hu, H. Peng, *J. Mater. Chem. A* **2016**, *4*, 10124.

[25] Q. Liu, G. Zhang, N. Chen, X. Feng, C. Wang, J. Wang, X. Jin, L. Qu, *Adv. Funct. Mater.* **2020**, *30*, 2002086.

[26] L. Q. Fan, J. Zhong, J. H. Wu, J. M. Lin, Y. F. Huang, *J. Mater. Chem. A* **2014**, *2*, 9011.

[27] B. Wang, J. A. Macia-Agullo, D. G. Prendiville, X. Zheng, D. Liu, Y. Zhang, S. W. Boettcher, X. Ji, G. D. Stucky, *J. Electrochem. Soc.* **2014**, *161*, A1090.

[28] C. John Zhang, L. McKeon, M. P. Kremer, S. H. Park, O. Ronan, A. Seral-Ascaso, S. Barwich, C. Coileáin, N. McEvoy, H. C. Nerl, B. Anasori, J. N. Coleman, Y. Gogotsi, V. Nicolosi, *Nat. Commun.* **2019**, *10*, 1795.

[29] S. Bellani, E. Petroni, A. E. Del Rio Castillo, N. Curreli, B. Martín-García, R. Oropesa-Nuñez, M. Prato, F. Bonaccorso, *Adv. Funct. Mater.* **2019**, *29*, 1807659.

[30] C. J. Zhang, M. P. Kremer, A. Seral-Ascaso, S. H. Park, N. McEvoy, B. Anasori, Y. Gogotsi, V. Nicolosi, *Adv. Funct. Mater.* **2018**, *28*, 1705506.

[31] Y. Wang, Y. Z. Zhang, D. Dubbink, J. E. ten Elshof, *Nano Energy* **2018**, *49*, 481.

[32] D. Song, F. Zare Bidoky, E. B. Secor, M. C. Hersam, C. Daniel Frisbie, *ACS Appl. Mater. Interfaces* **2019**, *11*, 9947.

[33] K. Brousse, S. Pinaud, S. Nguyen, P. F. Fazzini, R. Makarem, C. Josse, Y. Thimont, B. Chaudret, P. L. Taberna, M. Respaud, P. Simon, *Adv. Energy Mater.* **2020**, *10*, 1903136.

[34] X. Shi, S. Pei, F. Zhou, W. Ren, H. M. Cheng, Z. S. Wu, X. Bao, *Energy Environ. Sci.* **2019**, *12*, 1534.

[35] M. Qiu, P. Sun, G. Cui, Y. Tong, W. Mai, *ACS Nano* **2019**, *13*, 8246.

[36] M. De Volder, D. Reynaerts, C. Van Hoof, S. Tawfick, A. J. Hart, *Proc. IEEE Sensors* **2010**, 2369.

[37] G. Ge, Y. Lu, X. Qu, W. Zhao, Y. Ren, W. Wang, Q. Wang, W. Huang, X. Dong, *ACS Nano* **2020**, *14*, 218.

[38] J. Cao, Y. Zhao, Y. Xu, Y. Zhang, B. Zhang, H. Peng, *J. Mater. Chem. A* **2018**, *6*, 3355.

[39] J. Deng, C. Wang, G. Guan, H. Wu, H. Sun, L. Qiu, P. Chen, Z. Pan, H. Sun, B. Zhang, R. Che, H. Peng, *ACS Nano* **2017**, *11*, 8464.

[40] J. Li, L. Wang, Y. Zhao, S. Li, X. Fu, B. Wang, H. Peng, *Adv. Funct. Mater.* **2020**, *30*, 2001619.